Photocatalytic Hydrogen Evolution via Water Splitting: A Short Review

Yifan Zhang [1], Young-Jung Heo [1], Ji-Won Lee [1], Jong-Hoon Lee [1], Johny Bajgai [2], Kyu-Jae Lee [2,*] and Soo-Jin Park [1,*]

[1] Department of Chemistry and Chemical Engineering, Inha University, 100 Inharo, Incheon 22212, Korea; zyf9106@gmail.com (Y.Z.); heoyj1211@gmail.com (Y.-J.H.); lj529@naver.com (J.-W.L.); boy834@naver.com (J.-H.L.)

[2] Department of Environmental Medical Biology, Wonju College of Medicine, Yonsei University, Wonju 26426, Korea; johnybajgai@gmail.com

* Correspondence: medbio9@gmail.com (K.-J.L.); sjpark@inha.ac.kr (S.-J.P.); Tel.: +82-32-860-7234 (S.-J.P.); Fax: +82-32-860-5604 (S.-J.P.)

Abstract: Photocatalytic H_2 generation via water splitting is increasingly gaining attention as a viable alternative for improving the performance of H_2 production for solar energy conversion. Many methods were developed to enhance photocatalyst efficiency, primarily by modifying its morphology, crystallization, and electrical properties. Here, we summarize recent achievements in the synthesis and application of various photocatalysts. The rational design of novel photocatalysts was achieved using various strategies, and the applications of novel materials for H_2 production are displayed herein. Meanwhile, the challenges and prospects for the future development of H_2-producing photocatalysts are also summarized.

Keywords: photocatalysis; H_2 generation; water splitting; solar energy

1. Introduction

The development of renewable green energy sources is a critical challenge for modern society. H_2 is environmentally friendly, renewable, and considered to be an ideal candidate for an economically and socially sustainable fuel [1–6], and was previously regarded as an alternative energy source. Interestingly, some researchers also found that H_2-rich water has neuron effects owing to its antioxidant properties. Although the deep mechanism is not clear, more and more researchers made an effort to study the biological function of H_2 [7–21]. To date, almost all H_2 gas production processes in the industry are based on natural gas, coal, petroleum, or water electrolysis. These traditional preparation methods are limited due to the associated CO_2 emissions and high energy consumption. Hence, it is urgent to develop a low-cost method for efficient H_2 generation and, thus, support the emerging H_2 economy.

The sun provides an energy output of ~3×10^{24} J per year, which is approximately 12,000 times higher than the current energy demand. Therefore, solar energy can act as a sustainable alternative energy source in the future. To date, the transformation of solar energy into H_2 via water splitting is deemed as a desirable H_2 preparation method to solve the energy crisis [22,23].

The proper use of H_2 requires insight into the physical properties of H_2 molecules. As we know, the lengths and strengths of hydrogen bonds are exquisitely sensitive to temperature and pressure. Meanwhile, the charges of H_2 molecules also vary with temperature [24] because the spin direction of the nucleus in the H_2 molecule changes depending on the temperature, and an energy difference occurs between H_2 molecules. The *para*-H_2 fraction changes with temperature, and it is

necessary to understand the characteristics of H_2 molecules according to temperature [25]. During the reaction, hydrogen can be used safely at room temperature; however, it is rather dangerous in high-temperature environments.

As we know, H_2 gas, often called dihydrogen or molecular H_2, is a highly flammable gas with a wide range of concentrations between 4% and 75% by volume. Meanwhile, H_2 is the world's lightest gas. The density of H_2 is only 1/14 of that of air. At 0 °C, the density of H_2 is only 0.0899 g/L at standard atmospheric pressure, which is the smallest-molecular-weight substance; it is mainly used as a reducing agent. The enthalpy of combustion is about −286 kJ/mol, which can be displayed by the following equation: $2H_2(g) + O_2(g) \rightarrow 2H_2O(l) + 572$ kJ (286 kJ/mol). Currently, H_2 is the main industrial raw material and the most important industrial gas. It has various applications in the petrochemical, electronic, and metallurgical industry, as well as in food processing, float glass, fine organic synthesis, aerospace, and other fields. At the same time, H_2 is also an ideal secondary energy source. Owing to the properties of H_2, the aerospace industry uses liquid H_2 as fuel. Now, it is common to produce H_2 from water gas rather than using high-energy-consuming water. The produced H_2 is used in large quantities in the cracking reaction of the petrochemical industry and the production of ammonia. Unfortunately, all H_2 production methods are highly energy (thermal and electrical) demanding, which limits their application. Thus, it is crucial to find a new method of H_2 production.

Fujishima and Honda first reported photocatalytic water splitting using a TiO_2 electrode in 1972 [26]. Research on solar H_2 production attracted researchers in various fields, such as (1) chemists for the design and synthesis of various catalysts to investigate structure–property relationships; (2) physicists to fabricate semiconductor photocatalysts with novel electronic structures, as predicted by theoretical calculation; and (3) material scientists to construct unique photocatalytic materials with novel structures and morphologies [27–30]. When photocatalysts are illuminated at wavelengths which are suitable to their band gap energy, after the excitation, the charge carriers will either combine or transfer to the surface of the photocatalysts to participate in photocatalytic reactions. For the generation of efficient semiconductor photocatalysts, long-lived charge carriers and high stability are required [31–33].

Significant developments were made toward H_2 generation via water splitting over the last several decades by a number of talented researchers [34–38].

Herein, we attempt to sum up the advances achieved to date. Therefore, we briefly summarize the background related to various photocatalysts for H_2 generation and the achievements of high-efficiency photocatalysts. The main synthesis routes and modifications for adjusting the band structure to harvest light and enhance charge separation are also discussed.

2. Principle of H_2 Generation via Water Splitting

In the pioneering study by Fujishima and Honda [27], electrochemical cells were made up for the splitting of the water into H_2 and O_2, as shown in Figure 1. While the TiO_2 electrode was under ultraviolet (UV) light irradiation, water oxidation (oxygen evolution) occurred on its surface, while the reduction reaction (H_2 evolution) occurred on the surface platinum black electrode. With this study in mind, semiconductor photocatalysts were later developed by Bard et al. in their design of a novel photocatalytic system.
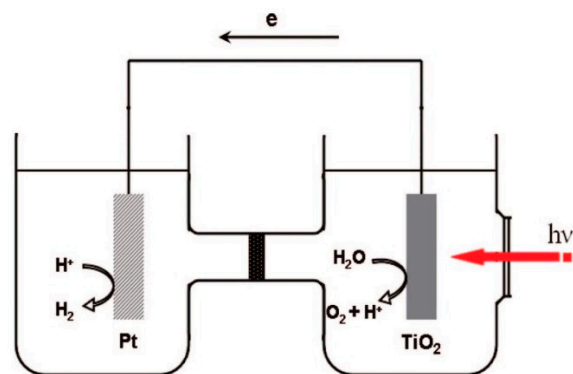
Figure 1. Schematic of a photoelectrochemical cell (PEC). Reproduced with permission from Reference [26]; copyright (1972), Nature Publishing Group.

Figure 2a shows a display of hydrogen evolution by photocatalysts. The photocatalytic reaction occurring on the semiconductor photocatalysts can be divided into three parts: (1) obtaining photons with energy exceeding that of the photocatalyst's band gap, generating electron and hole pairs; (2) separating carriers by migration in the semiconductor photocatalyst; and (3) reaction between these carriers and H_2O [39–46]. In addition, electron–hole pairs will combine with each other simultaneously. As shown in Figure 2b, while photocatalysts are involved in hydrogen evolution, the lowest position of the conduction band (CB) should be lower than the reduction position of H_2O/H_2, while the position of the valence band (VB) should be higher than the potential of H_2O/O_2 [47–50].
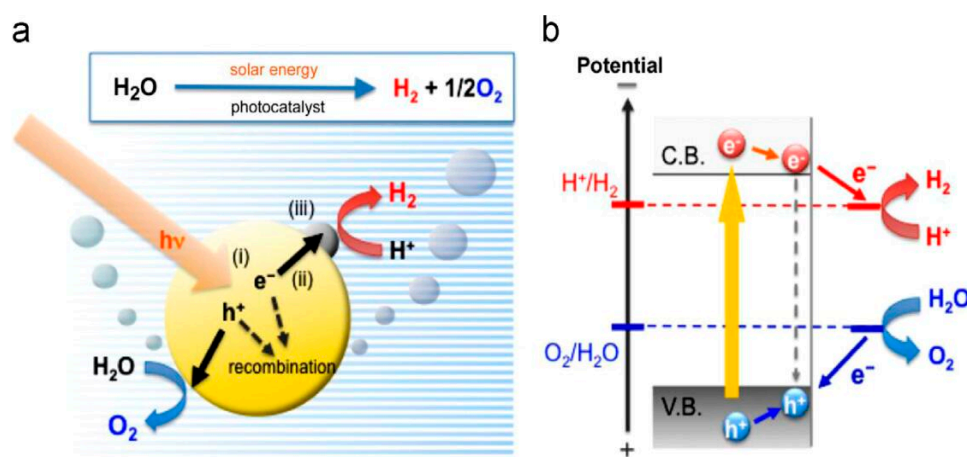
Figure 2. Schematic illustration of hydrogen evolution over photocatalysts. Reproduced with permission from Reference [39]; copyright (2014), Elsevier.

Various photocatalysts were reported to decompose water into H_2 and O_2 (Equation (1)). As we know, the hydrogen evolution reaction can be separated into two parts: oxidation for the evolution of O_2 (Equation (2)) and water reduction to produce H_2 (Equation (3)) [51–56]:

$$H_2O \rightarrow 2H_2 + O_2 \qquad\qquad \Delta E^0 = 1.23\ V \qquad\qquad (1)$$

$$H_2O \rightarrow 4H^+ + 4e^- + O_2 \qquad\qquad E^0 = +1.23\ V\ vs.\ NHE,\ pH = 0 \qquad\qquad (2)$$

$$4H^+ + 4e^- \rightarrow 2H_2 \qquad\qquad \Delta E^0 = 0\ V\ vs.\ NHE,\ pH = 0 \qquad\qquad (3)$$

3. Photocatalysts for Water Splitting

Many photocatalysts were created as photocatalysts for hydrogen evolution. Based on these species, they can be divided into three major parts: (1) graphene-based photocatalyst; (2)

graphitic carbon nitride (g-C3N4)-based photocatalysts; and (3) heterojunction photocatalysts (semiconductor–semiconductor or semiconductor–(metal, element)).

3.1. Graphene-Based Photocatalysts

Recently, graphene-based photocatalysts attracted significant attention for enhancing photocatalytic H_2 production performance. Graphene is used to enhance photocatalytic efficiency owing to its novel structure and electrochemical properties (Figure 3).
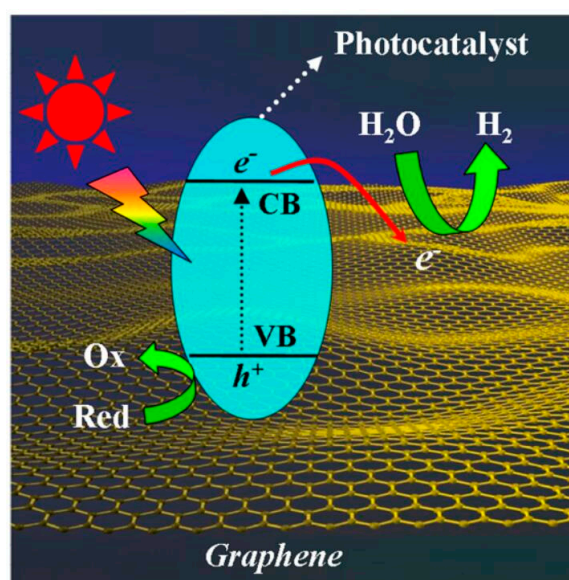
Figure 3. Proposed mechanism of graphene-based photocatalysts. Reproduced with permission from Reference [56]; copyright (2013), American Chemical Society.

To date, many reports regarding the synthesis of graphene-based photocatalysts with improved photocatalytic efficiency were published. Graphene is a well-known two-dimensional (2D) material, which can improve surface area, and its 2D membrane-like structure imparts unique electrochemical properties [57–60]. Generally speaking, photocatalysts prepared by simple physical mixing with graphene will involve only a bit of direct contact with the graphene sheets. This small amount of contact between the photocatalyst and graphene results in weak interactions and inhibits charge transfer rates. Hence, the synthesis of photocatalysts with more interactions is highly needed.

Previously, Kim et al. synthesized novel graphene oxide (GO)-TiO_2 photocatalysts [58] in 2013, comprising a core–shell nanostructure with enhanced photocatalytic efficiency (Figure 4). The improved H_2 production activity compared to that of TiO_2 revealed that the utilization of the core–shell structure enhanced photocatalytic efficiency. This novel structural design offers three-dimensional (3D) close contact between the materials and provides more active sites, which will enhance the charge separation rate and H_2 production efficiency [61–63].
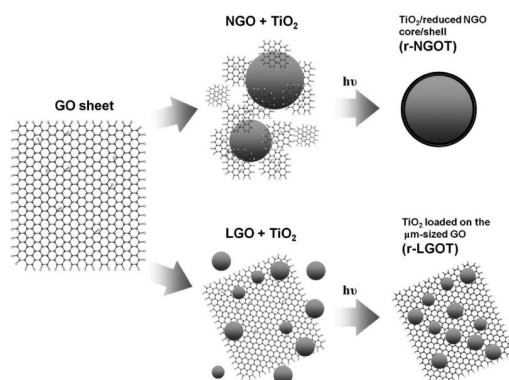
Figure 4. Schematic display of synthetic process of graphene oxide (GO)/TiO$_2$ and TiO$_2$/GO. Reproduced with permission from Reference [57]; copyright (2012), American Chemical Society.

Currently, many researchers are more interested in visible-light-driven photocatalysts, which are achieved using band-gap modification or taking graphene as a photosensitizer to broaden the visible-light adsorption range [64–66]. Significant efforts were conducted for building visible-light response systems because of the UV-only response of TiO$_2$, and its nontoxic properties [67]. Recently, it was found that graphene regulating TiO$_2$ involves visible-light adsorption activity. The carbon-layered structure of graphene with enriched π electrons forms bonds with titanium atoms. As a result, this strong interaction will shift the band position and reduce the band gap [68–70]. Lee et al. [71] also achieved a lower band gap using a graphene/TiO$_2$ photocatalyst. The improved photocatalytic efficiency of the graphene/TiO$_2$ composite owes to the band-gap regulation, which consequently promotes charge transfer rates through the graphene sheets.

3.2. g-C$_3$N$_4$-Based Photocatalysts

Currently, carbon-nitride-based photocatalysts receive significant attention for their photocatalytic H$_2$ generation owing to a unique electronic structure (Figure 5) [72–77]. This section summarizes recent significant achievements in building C$_3$N$_4$-based photocatalysts for H$_2$ evolution. Methods including nanostructure regulation, band-gap modification, dye sensitization, and heterojunction fabrication are highlighted herein.
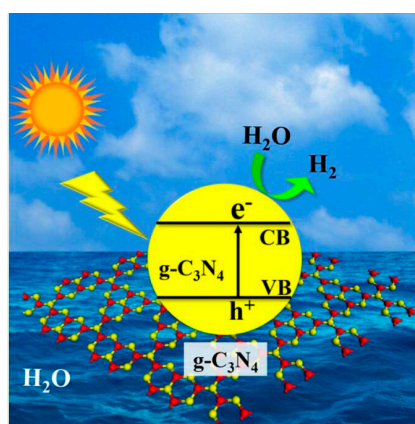
Figure 5. Proposed mechanism of graphitic carbon nitride (g-C$_3$N$_4$)-based photocatalysts. Reproduced with permission from Reference [72]; copyright (2014), American Chemical Society.

Recently, carbon nitride attracted significant attention following the pioneering research of Wang et al. in 2009 for photocatalytic hydrogen evolution [78,79]. The assumed structure of C$_3$N$_4$ is a 2D framework with the tri-*s*-triazine linked by tertiary amines (Figure 6); it is thermally stable and chemically stable. Pioneering studies regarded g-C$_3$N$_4$ as a visible-light-driven phorocatalyst with a

band gap of approximately 2.7 eV and an appropriate band position for water splitting [80–85]. Hence, g-C_3N_4 is an ideal candidate for photocatalytic H_2 evolution.
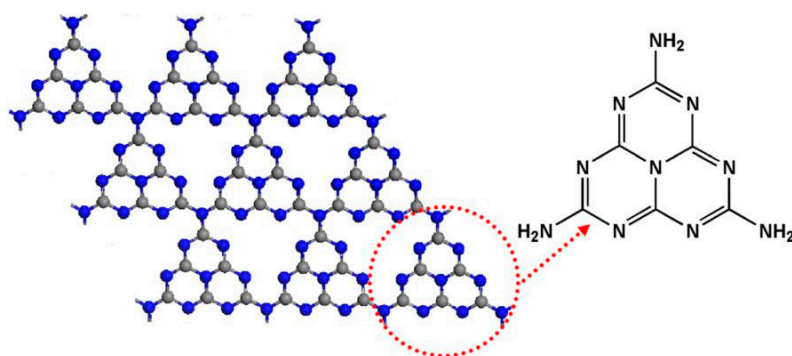
Figure 6. Schematic display of the structure of g-C_3N_4. Reproduced with permission from Reference [72]; copyright (2014), American Chemical Society.

H_2 generation performance using g-C_3N_4 can be promoted with noble-metal particles such as Au or Pd, which obtain electrons in the CB to inhibit the charge recombination rate [86–90]. Many researchers are developing metal-free photocatalysts for H_2 evolution, and recent reports involved the introduction of non-noble-metal catalysts into g-C_3N_4 photocatalysts, displaying enhanced photocatalytic performance compared to noble-metal catalysts [91–95]. Hou et al. [86] synthesized MoS_2/g-C_3N_4 composite photocatalysts (Figure 7) in 2018. MoS_2/g-C_3N_4 increased the surface area and decreased the barrier when the electrons transported, thereby improving the charge transfer rate. The formation of band alignment enabled electron transfer from the CB (g-C_3N_4) to MoS_2. Therefore, the MoS_2/gC_3N_4 nanojunction significantly enhanced H_2 evolution efficiency, achieving the highest H_2 evolution rate and an optimum quantum efficiency of up to 2.1% (420 nm), which was higher than g-C_3N_4/Pt.
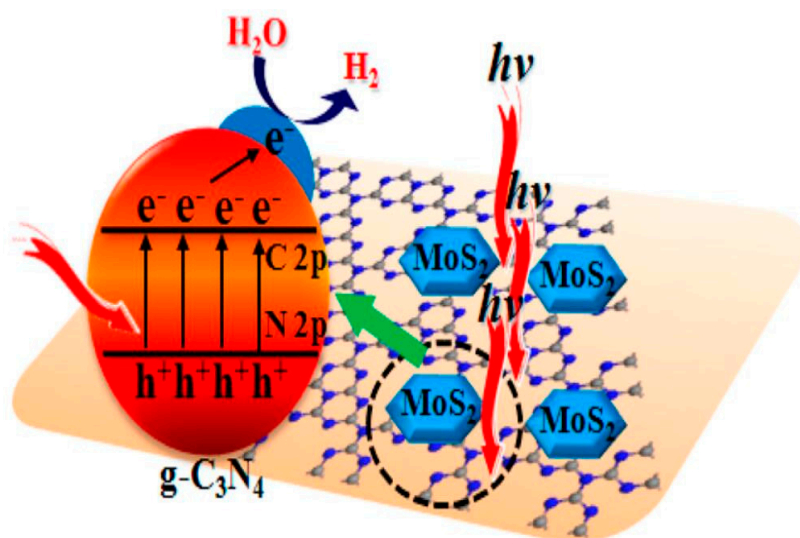
Figure 7. Schematic display of charge transfer on MoS_2/g-C_3N_4 heterostructures during water splitting. Reproduced with permission from Reference [72]; copyright (2014), American Chemical Society.

3.3. Metal-Loading-Based Photocatalysts

Metal loading is also regarded as a useful method for photocatalytic enhancement. Song et al. [96] constructed Ag-rGO-TiO_2 composite photocatalysts (Figure 8) in 2018. In order to analyze the photocatalytic mechanism of the architectural Ag-TiO_2 and Ag-rGO-TiO_2 composites, their structures with Ag nanocubes for light absorption and TiO_2 nanosheets were well displayed. The difference

between Ag-TiO$_2$ and Ag-rGO-TiO$_2$ is the interface between Ag nanocubes and TiO$_2$ nanosheets, which enhances the electron transfer capability. For Ag-TiO$_2$, the direct contact between the two materials results in the formation of Ag (100)/(001) TiO$_2$ interface. Meanwhile, for Ag-rGO-TiO$_2$, both Ag(100)/rGO and rGO/(001) TiO$_2$ interfaces are formed by rGO. As mentioned above, the synergistic effect of Ag(100)/rGO and rGO/(001)TiO$_2$ interfaces, rather than the Ag(100)/(001) TiO$_2$ interface, offers quicker electron transfer. As shown in Figure 8, no Schottky barrier is formed between Ag and TiO$_2$, and the hot electrons on the surface of TiO$_2$ flow back to Ag and then recombine with holes. Meanwhile, for the Ag-rGO-TiO$_2$ sample, no barrier is necessary to facilitate the electron transfer. The electrons generated on the surface of Ag nanocubes with smaller work function flow to rGO via a contact so as to equilibrate the electron Fermi distribution on the interface [97,98]. Moreover, the rGO nanosheets can act as conductive channels, further transferring the electron to the rGO/TiO$_2$ interface. Owing to the light absorption of rGO, the transferred electrons within the rGO nanosheets can be further transferred to the CB of TiO$_2$ under light excitation. The proposed photocatalytic mechanism of Ag-rGO-TiO$_2$ is illustrated in Figure 8.
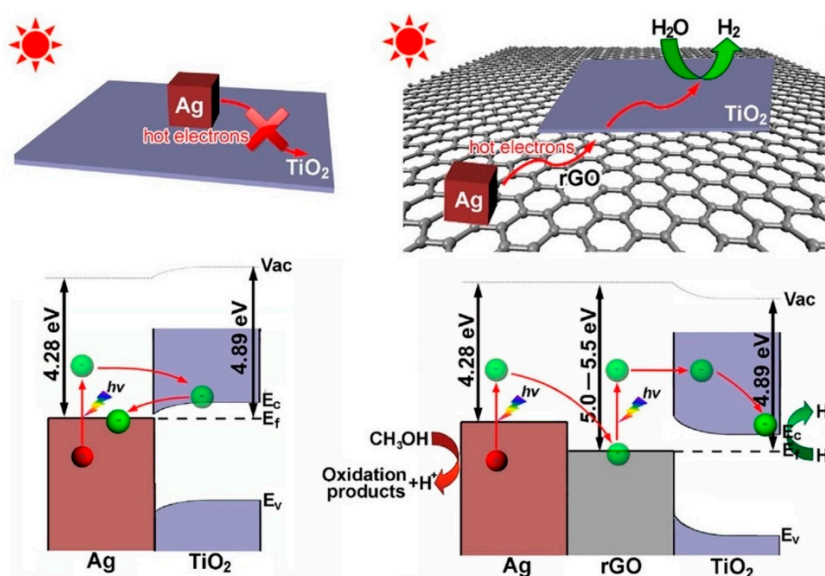
Figure 8. Schematic illustrating photocatalytic mechanism for Ag-TiO$_2$ and Ag-rGO-TiO$_2$ samples under visible-light irradiation. Reproduced with permission from Reference [95]; copyright (2018), Elsevier.

3.4. Z-Scheme Photocatalysts

An illustration of Z-scheme water splitting is shown in Figure 9. During an H$_2$ evolution reaction, the reactions which happen on the surface of photocatalysts include the reduction of protons by CB electrons and the oxidation of an electron donor (D) by VB holes, yielding the corresponding electron acceptor (A), as follows:

$$2H^+ + 2e^- \rightarrow H_2 \; (photoreduction \; of \; H^+ \; to \; H_2)$$

$$D + nh^+ \rightarrow A \; (photooxidation \; of \; D \; to \; A)$$

On the other hand, the forward reactions on an O$_2$ evolution photocatalyst are as follows:

$$A + ne^- \rightarrow D \; (photoreduction \; of \; A \; to \; D)$$

$$2H_2O + 4h^+ \rightarrow O_2 + 4H^+ \; ((photooxidation \; of \; H_2O \; to \; O_2)$$
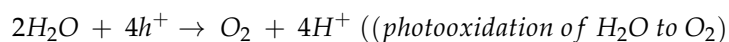
where the electron acceptor generated by the paired H_2 evolution photocatalyst is converted to D, and the water oxidation process occurs via the valence band holes. Thus, the water-splitting process can be achieved.
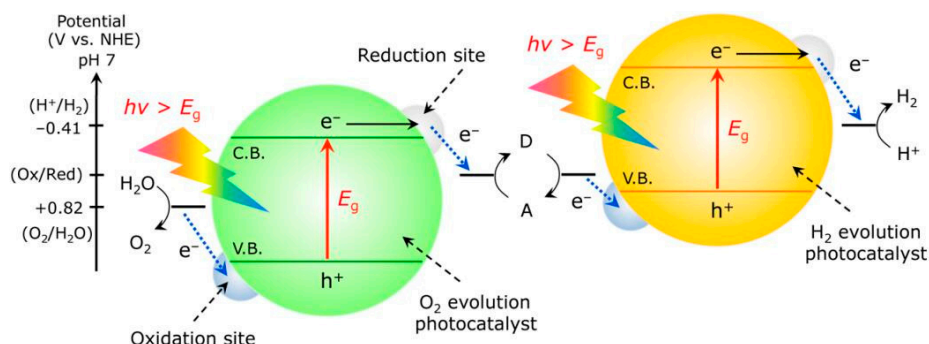
Figure 9. Diagram of photocatalytic water splitting using a Z-Scheme system. Reproduced with permission from Reference [98]; Copyright (2010), American Chemical Society.

Amal et al. reported a Z-scheme photocatalytic water-splitting system using $Ru/SrTiO_3$ and partially reduced GO (PRGO)/$BiVO_4$ (Figure 10) in 2011 [100]. As described in the report, the PRGO/$BiVO_4$ (O_2 photocatalyst) and $Ru/SrTiO_3$:Rh (H_2 photocatalyst) were attached due to surface charge modification in acidic conditions, as depicted in Figure 10. Under irradiation, electrons are excited from the VB ($BiVO_4$) or an impurity level in Rh ($Ru/SrTiO_3$:Rh) to the CB. We can indicate that the PRGO does not contribute to the electron and hole generation. In other words, the RGO in this work acts as an electron conductor. PRGO transfers the electrons from the CB of $BiVO_4$ to the $Ru/SrTiO_3$:Rh. Meanwhile, the electrons in $Ru/SrTiO_3$:Rh reduce the water to H_2 on the surface of the Ru co-catalyst, while the holes left in $BiVO_4$ oxidize the water to O_2. Additionally, the PRGO provides a pathway for photogenerated electrons in the $BiVO_4$ photocatalyst. Each reaction can migrate as follows: reduction of water, transfer of electrons to PRGO, and transfer of holes to PRGO for oxidation. Because the majority of the photocatalyst surface is surrounded by water and only relatively small portions are in contact with PRGO [101], most electrons in $Ru/SrTiO_3$:Rh and holes in $BiVO_4$ are used for water splitting.
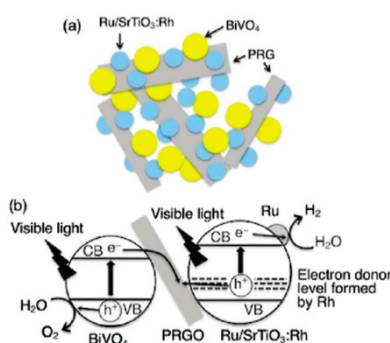
Figure 10. (**a**) Schematic display of a suspension of $Ru/SrTiO_3$ and partially reduced GO (PRGO)/$BiVO_4$ in water. (**b**) Mechanism of water splitting using Z-scheme system consisting of $Ru/SrTiO_3$ and PRGO/$BiVO_4$ under irradiation. Reproduced with permission from Reference [99]; copyright (2018), American Chemical Society.

3.5. Defect Engineering Photocatalyst

Among the various photocatalyst designs, the defect engineering strategy is regarded as an important way of modifying the photocatalysts. Defects are places where the atoms or molecules in the materials are disrupted, and they greatly influence photocatalytic performance. The defects in the lattice of photocatalysts not only act as an electron–hole recombination center, but also break

the electronic structure and display a scattering center for electron and hole travel. Nevertheless, the positive effect of defects in photocatalytic performance enhancement were also recognized with the development of defect photocatalysts and the development of the photocatalytic field.

Chen et al. reported the synthesis of a bismuth subcarbonate ($Bi_2O_2CO_3$, BOC) with controllable defect density (BOC-X) (Figure 11) in 2018. The BOC-X with defect density displayed a photocatalytic nitrogen fixation of 957 $\mu mol \cdot L^{-1}$ under irradiation within 4 h, which was 9.4 times higher than that of pristine BOC. This photocatalytic performance enhancement of BOC-X can be attributed to the surface defects. These defects contribute to the defect levels in the forbidden band, which improves the light harvest percentage. Meanwhile, surface defects can also inhibit the electron–hole recombination rate to promote the separation efficiency of charge carriers. Photocatalytic nitrogen fixation by BOC-X is displayed in Figure 11. If the light energy is higher than the band-gap energy, the electrons on the VB surface of BOC-X are transferred to the CB and react with N_2 to form NH_3. Moreover, some of the VB electrons are transferred to the defect level and then react with N_2. However, if the light energy is lower than the band-gap energy, the electrons of BOC-X are also excited from VB to the defect level and then participate in the reaction. Defects modulate the band gap of BOC-X and improve the light absorption range, thereby enhancing the carrier transport, and leading to photocatalytic enhancement.
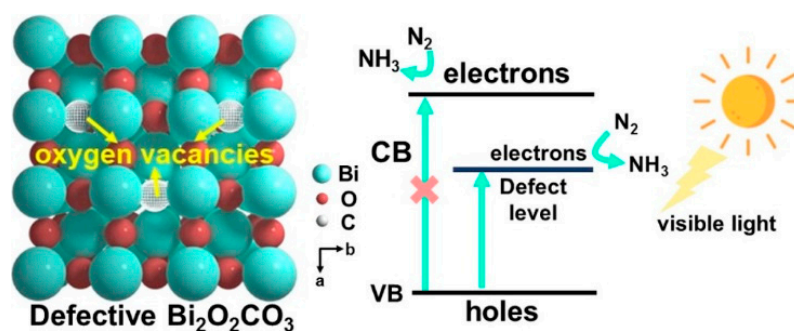
Figure 11. Mechanism of photocatalytic nitrogen fixation on defective $Bi_2O_2CO_3$. Reproduced with permission from Reference [101]; copyright (2010), American Chemical Society.

3.6. Heterojunction Photocatalysts

During the H_2 evolution reaction, the formed electron–hole charges are transferred to the surface of the photocatalyst for the next step of the reaction or recombine with each other [102–106]. To better reveal this point, we assumed it as a simple case [107]: the influence of gravity on a man jumping (Figure 12a,b). When a man (electron) jumps from the ground (VB) to the sky (CB), it can return to the floor immediately (recombination of the electron and hole) owing to gravity. In order to let the people rise off the floor (separation of the charge carrier pairs), an instrument (semiconductor B) can be used (Figure 12c,d). Subsequently, the previously mentioned people can drop to the instrument rather than the ground (inhibition of the electron and hole pair recombination). Although the inhibition of electron–hole recombination rate is an urgent issue, it can be achieved via suitable construction of materials. Many methods were conducted to achieve better electron–hole pair separation rate, such as element combining [108,109], metal doping [110,111], or the use of heterojunctions [112,113]. Among these strategies, heterojunctions were proven to be the most desirable method for achieving efficient photocatalysis due to their improved separation ability of electron–hole pairs (Figure 12d).
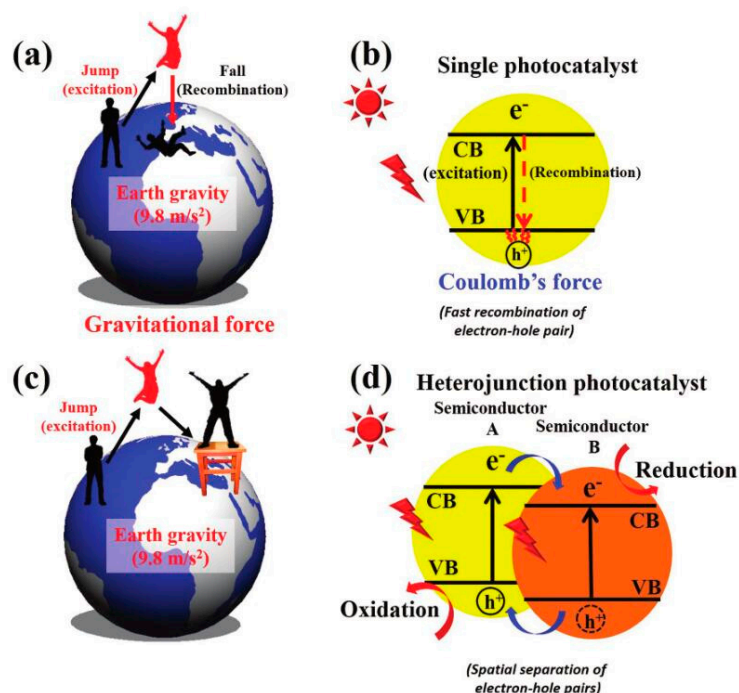
Figure 12. Schematic display of (**a**) the influence of gravity on a person jumping, (**b**) electron–hole pair combination using a photocatalyst, (**c**) utilization of a stool to keep the person from returning to the ground, (**d**) electron–hole pairs separated in composite catalyst. Reproduced with permission from Reference [105]; copyright (2010), John Wiley & Sons, Inc.

A heterojunction is regarded as the connection between two kinds of photocatalysts with different band structures, which leads to a new band arrangement [114,115]. Generally, three kinds of composite photocatalysts are developed (Figure 13). As shown in Figure 13a, the CB and VB of A are a bit over and under the band position of B, respectively [116]. As a result, when the light irradiates, the generated electrons and holes are transferred to the CB and VB of B. Because the generated electrons and holes move to the same photocatalyst, the recombination rate of electron–hole pairs is not efficiently inhibited. The photocatalytic process happens on photocatalyst B with a mild potential requirement; thus, the photocatalytic ability of the photocatalyst using this heterojunction will be lower than others. As dispalyed in Figure 13b, the band positions of CB and VB are over that of photocatalyst B. Hence, during the photocatalytic reaction, the generated electron moves to photocatalyst B, while the holes are transferred to photocatalyst A, which leads to the formation of long lived electron–hole pairs [117–119]. Parallel to Figure 13a, the photocatalytic performance of the type-II composite photocatalysts is inhibited by the redox process occurring on B. Meanwhile, as displayed in Figure 13c, the band structure of type-III composite photocatalysts is parallel to type II, apart from the interlaced gap changing into non-overlapping band gaps [120,121]. Thus, the generated electron–hole pairs cannot be transferred between the two photocatalysts, resulting in them being inappropriate for long lived electron–hole pair separation. We can determine that the type-II heterojunctions are desirable for enhancing redox ability due to their optimum structure for long-lived electron–hole separation. In previous reports, great efforts were conducted to synthesize type-II composite photocatalysts, including g-C_3N_4/TiO_2 [122], WO_3/$BiVO_4$ [123], WO_3/g-C_3N_4 [124], and $BiPO_4$/g-C_3N_4 [125].
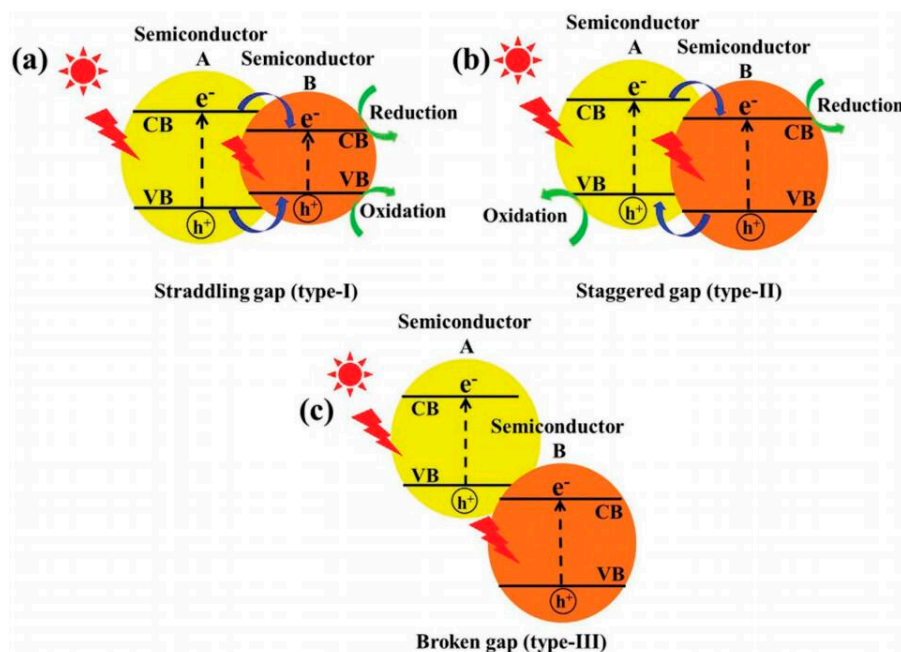
Figure 13. Schematic display of three kinds of electron–hole pair separation among composite photocatalysts: (**a**) type-I, (**b**) type-II, (**c**) type-III heterojunctions. Reproduced with permission from Reference [105]; copyright (2017), John Wiley & Sons, Inc.

Yu et al. designed CdS/NiS composites photocatalysts using various heterojunctions in 2012, which greatly enhanced the hydrogen evolution performance. As shown in Figure 14a, around 20 nm of NiS particles were loaded onto the CdS uniformly, which supported a close connection between CdS and NiS. The formation of p–n heterojunctions facilitates charge transfer between the NiS and CdS, and inhibits charge-carrier recombination (Figure 14b,c). We can see that the holes left on the n-type catalyst are transferred to the p-type catalyst, providing a negative specie. The electron–hole pair distribution keeps moving until a Fermi-level equilibrium is achieved [126–128]. The generated active species move through the internal electric field of the composite photocatalysts, resulting in long-lived electron–hole pair separation rates. Thus, the electron–hole recombination rate is efficiently inhibited owing to the synergistic effect between the two photocatalysts. The photocatalytic H_2 production rate over CdS/NiS composite photocatalysts with 5 wt.% NiS was found to be higher than that of the CdS and 1 wt.% Pt/CdS (Figure 14d). More NiS doping resulted in a reduction in photocatalytic efficiency due to NiS catalysts reducing the number of redox sites during the reaction.
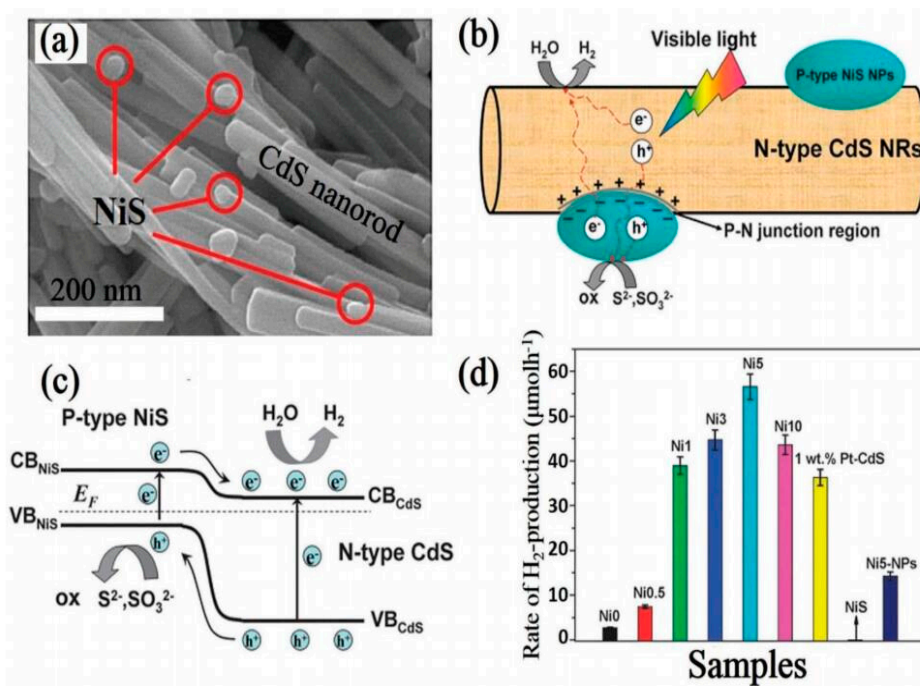
Figure 14. (**a**) SEM image of CdS/NiS composite catalysts; (**b**,**c**) illustration of electron–hole pairs with CdS/NiS composite photocatalysts; (**d**) contrast of photocatalytic efficiency of CdS with different NiS content. Reproduced with permission from Reference [105]; copyright (2017), John Wiley & Sons, Inc.

4. Summary and Perspectives

Over the last several decades, photocatalysis was shown to be a promising method for H_2 production. Even though the principles controlling photocatalytic activity in the developed semiconductors were identified, several aspects remain unclear. Therefore, practical applications and the commercialization of photocatalytic H_2 production require further research. Meanwhile, the charge transfer among photocatalysts due to the influence of structure and electrochemical properties is also not very clear, while the influence of various preparation methods on the catalytic performance is not well understood. The development of improved photocatalysts will benefit from advances in science. Improved building of novel co-catalysts will arise from using efficient catalysts. Many researches are underway investigating new synthesis methods for sample preparation and novel system construction. Herein, we concluded the most prominent achievements associated with H_2 production via photocatalysis. We hope this report will assist further research efforts regarding the development of photocatalysts.

References

1. Park, S.J.; Lee, S.Y. A study on hydrogen-storage behaviors of nickel-loaded mesoporous MCM-41. *J. Colloid Interface Sci.* **2010**, *346*, 194–198. [CrossRef] [PubMed]
2. Catapan, R.C.; Cancino, L.R.; Oliveira, A.A.M.; Schwarz, C.O.; Nitschke, H.; Frank, T. Potential for onboard hydrogen production in an direct injection ethanol fueled spark ignition engine with EGR. *Fuel* **2018**, *234*, 441–446. [CrossRef]

3. Im, J.S.; Park, S.-J.; Kim, T.; Lee, Y.-S. Hydrogen storage evaluation based on investigations of the catalyticproperties of metal/metal oxides in electrospun carbon fibers. *Int. J. Hydrogen Energy* **2009**, *34*, 3382–3388. [CrossRef]

4. Park, S.-J.; Lee, S.-Y. Hydrogen storage behaviors of platinum-supported multi-walled carbon nanotubes. *Int. J. Hydrogen Energy* **2010**, *35*, 13048–13054. [CrossRef]

5. Lee, S.-Y.; Park, S.-J. Effect of platinum doping of activated carbon on hydrogen storage behaviors of metal-organic frameworks-5. *Int. J. Hydrogen Energy* **2011**, *36*, 8381–8387. [CrossRef]

6. Baykara, S.Z. Hydrogen: A brief overview on its sources, production and environmental impact. *Int. J. Hydrogen Energy* **2018**, *43*, 10605–10614. [CrossRef]

7. Chen, M.; Cui, W.; Zhu, K.; Xie, Y.; Zhang, C.; Shen, W. Hydrogen-rich water alleviates aluminum-induced inhibition of root elongation in alfalfa via decreasing nitric oxide production. *J. Hazard. Mater.* **2014**, *267*, 40–47. [CrossRef] [PubMed]

8. Cui, W.; Gao, C.; Fang, P.; Lin, G.; Shen, W. Alleviation of cadmium toxicity in Medicago sativa by hydrogen-rich water. *J. Hazard. Mater.* **2013**, *260*, 715–724. [CrossRef] [PubMed]

9. Gao, Q.; Song, H.; Wang, X.T.; Liang, Y.; Xi, Y.J.; Gao, Y.; Guo, Q.J.; LeBaron, T.; Luo, Y.X.; Li, S.C.; et al. Molecular hydrogen increases resilience to stress in mice. *Sci. Rep.* **2017**, *7*, 9625. [CrossRef]

10. Giuliani, D.; Ottani, A.; Zaffe, D.; Galantucci, M.; Strinati, F.; Lodi, R.; Guarini, S. Hydrogen sulfide slows down progression of experimental Alzheimer's disease by targeting multiple pathophysiological mechanisms. *Neurobiol. Learn. Mem.* **2013**, *104*, 82–91. [CrossRef]

11. Huang, C.S.; Kawamura, T.; Toyoda, Y.; Nakao, A. Recent advances in hydrogen research as a therapeutic medical gas. *Free Radic. Res.* **2010**, *44*, 971–982. [CrossRef] [PubMed]

12. Kumar, R.; Kumar, A.; Langstrom, B.; Darreh-Shori, T. Discovery of novel choline acetyltransferase inhibitors using structure-based virtual screening. *Sci. Rep.* **2017**, *7*, 16287. [CrossRef]

13. Li, J.; Wang, C.; Zhang, J.H.; Cai, J.M.; Cao, Y.P.; Sun, X.J. Hydrogen-rich saline improves memory function in a rat model of amyloid-beta-induced Alzheimer's disease by reduction of oxidative stress. *Brain Res.* **2010**, *1328*, 152–161. [CrossRef]

14. Luo, Q.; Lin, Y.X.; Yang, P.P.; Wang, Y.; Qi, G.B.; Qiao, Z.Y.; Li, B.N.; Zhang, K.; Zhang, J.P.; Wang, L.; et al. A self-destructive nanosweeper that captures and clears amyloid beta-peptides. *Nat. Commun.* **2018**, *9*, 1802. [CrossRef] [PubMed]

15. Nagata, K.; Nakashima-Kamimura, N.; Mikami, T.; Ohsawa, I.; Ohta, S. Consumption of molecular hydrogen prevents the stress-induced impairments in hippocampus-dependent learning tasks during chronic physical restraint in mice. *Neuropsychopharmacol. Off. Publ. Am. Coll. Neuropsychopharmacol.* **2009**, *34*, 501–508. [CrossRef]

16. Nakayama, M.; Itami, N.; Suzuki, H.; Hamada, H.; Yamamoto, R.; Tsunoda, K.; Osaka, N.; Nakano, H.; Maruyama, Y.; Kabayama, S.; et al. Novel haemodialysis (HD) treatment employing molecular hydrogen (H2)-enriched dialysis solution improves prognosis of chronic dialysis patients: A prospective observational study. *Sci. Rep.* **2018**, *8*, 254. [CrossRef] [PubMed]

17. Nishimaki, K.; Asada, T.; Ohsawa, I.; Nakajima, E.; Ikejima, C.; Yokota, T.; Kamimura, N.; Ohta, S. Effects of Molecular Hydrogen Assessed by an Animal Model and a Randomized Clinical Study on Mild Cognitive Impairment. *Curr. Alzheimer Res.* **2018**, *15*, 482–492. [CrossRef] [PubMed]

18. Ohsawa, I.; Ishikawa, M.; Takahashi, K.; Watanabe, M.; Nishimaki, K.; Yamagata, K.; Katsura, K.; Katayama, Y.; Asoh, S.; Ohta, S. Hydrogen acts as a therapeutic antioxidant by selectively reducing cytotoxic oxygen radicals. *Nat. Med.* **2007**, *13*, 688–694. [CrossRef]

19. Xiao, H.W.; Li, Y.; Luo, D.; Dong, J.L.; Zhou, L.X.; Zhao, S.Y.; Zheng, Q.S.; Wang, H.C.; Cui, M.; Fan, S.J. Hydrogen-water ameliorates radiation-induced gastrointestinal toxicity via MyD88's effects on the gut microbiota. *Exp. Mol. Med.* **2018**, *50*, e433. [CrossRef]

20. Zhang, L.M.; Jiang, C.X.; Liu, D.W. Hydrogen sulfide attenuates neuronal injury induced by vascular dementia via inhibiting apoptosis in rats. *Neurochem. Res.* **2009**, *34*, 1984–1992. [CrossRef] [PubMed]

21. Zhang, Y.; Su, W.J.; Chen, Y.; Wu, T.Y.; Gong, H.; Shen, X.L.; Wang, Y.X.; Sun, X.J.; Jiang, C.L. Effects of hydrogen-rich water on depressive-like behavior in mice. *Sci. Rep.* **2016**, *6*, 23742. [CrossRef] [PubMed]

22. Liu, S.; Xin, Z.-J.; Lei, Y.-J.; Yang, Y.; Yan, X.-Y.; Lu, Y.-B.; Li, C.-B.; Wang, H.-Y. Thin Copper-Based Film for Efficient Electrochemical Hydrogen Production from Neutral Aqueous Solutions. *ACS Sustain. Chem. Eng.* **2017**, *5*, 7496–7501. [CrossRef]

23. Wang, Z.; Yang, X.; Yang, T.; Zhao, Y.; Wang, F.; Chen, Y.; Zeng, J.H.; Yan, C.; Huang, F.; Jiang, J.-X. Dibenzothiophene Dioxide Based Conjugated Microporous Polymers for Visible-Light-Driven Hydrogen Production. *ACS Catal.* **2018**, *8*, 8590–8596. [CrossRef]

24. Zhu, K.; Kang, S.-Z.; Qin, L.; Han, S.; Li, G.; Li, X. Novel and Highly Active Potassium Niobate-Based Photocatalyst for Dramatically Enhanced Hydrogen Production. *J. Am. Chem. Soc.* **2005**, *127*, 11447–11453. [CrossRef]

25. Hibino, T.; Kobayashi, K.; Ito, M.; Ma, Q.; Nagao, M.; Fukui, M.; Teranishi, S. Kinetics of the Interconversion of Parahydrogen and Orthohydrogen Catalyzed by Paramagnetic Complex Ions. *J. Am. Chem. Soc.* **2005**, *127*, 11447–11453.

26. Fujishima, A.; Honda, K. Electrochemical Photolysis of Water at a Semiconductor Electrode. *Nature* **1972**, *238*, 37–38. [CrossRef] [PubMed]

27. Zhang, P.; Song, T.; Wang, T.; Zeng, H. In-situ synthesis of Cu nanoparticles hybridized with carbon quantum dots as a broad spectrum photocatalyst for improvement of photocatalytic H_2 evolution. *Appl. Catal. B Environ.* **2017**, *206*, 328–335. [CrossRef]

28. Zhang, P.; Song, T.; Wang, T.; Zeng, H. Plasmonic Cu nanoparticle on reduced graphene oxide nanosheet support: An efficient photocatalyst for improvement of near-infrared photocatalytic H_2 evolution. *Appl. Catal. B Environ.* **2018**, *225*, 172–179. [CrossRef]

29. Zhang, P.; Wang, T.; Zeng, H. Design of Cu-Cu_2O/g-C_3N_4 nanocomponent photocatalysts for hydrogen evolution under visible light irradiation using water-soluble Erythrosin B dye sensitization. *Appl. Surf. Sci.* **2017**, *391*, 404–414. [CrossRef]

30. Zhang, P.; Song, T.; Wang, T.; Zeng, H. Effectively extending visible light absorption with a broad spectrum sensitizer for improving the H_2 evolution of in-situ Cu/g-C_3N_4 nanocomponents. *Int. J. Hydrogen Energy* **2017**, *42*, 14511–14521. [CrossRef]

31. Zhang, Y.; Park, M.; Kim, H.Y.; Ding, B.; Park, S.J. A facile ultrasonic-assisted fabrication of nitrogen-doped carbon dots/BiOBr up-conversion nanocomposites for visible light photocatalytic enhancements. *Sci. Rep.* **2017**, *7*, 45086. [CrossRef] [PubMed]

32. Zhang, Y.; Park, S.-J. Bimetallic AuPd alloy nanoparticles deposited on MoO_3 nanowires for enhanced visible-light driven trichloroethylene degradation. *J. Catal.* **2018**, *361*, 238–247. [CrossRef]

33. Zhang, Y.; Park, S.-J. Au–pd bimetallic alloy nanoparticle-decorated $BiPO_4$ nanorods for enhanced photocatalytic oxidation of trichloroethylene. *J. Catal.* **2017**, *355*, 1–10. [CrossRef]

34. Yu, H.; Xue, Y.; Hui, L.; Zhang, C.; Li, Y.; Zuo, Z.; Zhao, Y.; Li, Z.; Li, Y. Efficient Hydrogen Production on a 3D Flexible Heterojunction Material. *Adv. Mater.* **2018**, *30*, e1707082. [CrossRef]

35. Zhang, P.; Song, T.; Wang, T.; Zeng, H. Fabrication of a non-semiconductor photocatalytic system using dendrite-like plasmonic CuNi bimetal combined with a reduced graphene oxide nanosheet for near-infrared photocatalytic H_2 evolution. *J. Mater. Chem. A* **2017**, *5*, 22772–22781. [CrossRef]

36. Lin, L.; Ren, W.; Wang, C.; Asiri, A.M.; Zhang, J.; Wang, X. Crystalline carbon nitride semiconductors prepared at different temperatures for photocatalytic hydrogen production. *Appl. Catal. B Environ.* **2018**, *231*, 234–241. [CrossRef]

37. Im, J.S.; Kwon, O.; Kim, Y.H.; Park, S.-J.; Lee, Y.-S. The effect of embedded vanadium catalyst on activated electrospun CFs for hydrogen storage. *Microporous Mesoporous Mater.* **2008**, *115*, 514–521. [CrossRef]

38. Yi, H.; Huang, D.; Qin, L.; Zeng, G.; Lai, C.; Cheng, M.; Ye, S.; Song, B.; Ren, X.; Guo, X. Selective prepared carbon nanomaterials for advanced photocatalytic application in environmental pollutant treatment and hydrogen production. *Appl. Catal. B Environ.* **2018**, *239*, 408–424. [CrossRef]

39. Ismail, A.A.; Bahnemann, D.W. Photochemical splitting of water for hydrogen production by photocatalysis: A review. *Sol. Energy Mater. Sol. Cells* **2014**, *128*, 85–101. [CrossRef]

40. Cai, J.; Shen, J.; Zhang, X.; Ng, Y.H.; Huang, J.; Guo, W.; Lin, C.; Lai, Y. Light-Driven Sustainable Hydrogen Production Utilizing TiO_2 Nanostructures: A Review. *Small Methods* **2018**, 1800184. [CrossRef]

41. Ventura-Espinosa, D.; Sabater, S.; Carretero-Cerdán, A.; Baya, M.; Mata, J.A. High Production of Hydrogen on Demand from Silanes Catalyzed by Iridium Complexes as a Versatile Hydrogen Storage System. *ACS Catal.* **2018**, *8*, 2558–2566. [CrossRef]

42. Ji, L.; Lv, C.; Chen, Z.; Huang, Z.; Zhang, C. Nickel-Based (Photo) Electrocatalysts for Hydrogen Production. *Adv. Mater.* **2018**, *30*, e1705653. [CrossRef] [PubMed]

43. Ma, Y.; Dong, X.; Wang, Y.; Xia, Y. Decoupling Hydrogen and Oxygen Production in Acidic Water Electrolysis Using a Polytriphenylamine-Based Battery Electrode. *Angewandte Chem.* **2018**, *57*, 2904–2908. [CrossRef] [PubMed]

44. Wang, B.; Zeng, C.; Chu, K.H.; Wu, D.; Yip, H.Y.; Ye, L.; Wong, P.K. Enhanced Biological Hydrogen Production from Escherichia coli with Surface Precipitated Cadmium Sulfide Nanoparticles. *Adv. Energy Mater.* **2017**, *7*, 1700611. [CrossRef]

45. Xue, Z.; Shen, Y.; Li, P.; Zhang, Y.; Li, J.; Qin, B.; Zhang, J.; Zeng, Y.; Zhu, S. Key Role of Lanthanum Oxychloride: Promotional Effects of Lanthanum in NiLaOy/NaCl for Hydrogen Production from Ethyl Acetate and Water. *Small* **2018**, *14*, e1800927. [CrossRef] [PubMed]

46. Zhang, Y.; Yang, H.M.; Park, S.-J. Synthesis and characterization of nitrogen-doped TiO_2 coatings on reduced graphene oxide for enhancing the visible light photocatalytic activity. *Curr. Appl. Phys.* **2018**, *18*, 163–169. [CrossRef]

47. Zhang, Y.; Park, M.; Kim, H.-Y.; Park, S.-J. In-situ synthesis of graphene oxide/BiOCl heterostructured nanofibers for visible-light photocatalytic investigation. *J. Alloy Compd.* **2016**, *686*, 106–114. [CrossRef]

48. Huang, J.; Li, G.; Zhou, Z.; Jiang, Y.; Hu, Q.; Xue, C.; Guo, W. Efficient photocatalytic hydrogen production over Rh and Nb codoped TiO_2 nanorods. *Chem. Eng. J.* **2018**, *337*, 282–289. [CrossRef]

49. Kim, W.; Monllor-Satoca, D.; Chae, W.-S.; Mahadik, M.A.; Jang, J.S. Enhanced photoelectrochemical and hydrogen production activity of aligned CdS nanowire with anisotropic transport properties. *Appl. Surf. Sci.* **2019**, *463*, 339–347. [CrossRef]

50. Han, J.; Liu, Y.; Dai, F.; Zhao, R.; Wang, L. Fabrication of CdSe/CaTiO₃ nanocomposties in aqueous solution for improved photocatalytic hydrogen production. *Appl. Surf. Sci.* **2018**, *459*, 520–526. [CrossRef]

51. Zhang, Y.; Park, M.; Kim, H.Y.; Ding, B.; Park, S.-J. In-situ synthesis of nanofibers with various ratios of BiOClx/BiOBry/BiOIz for effective trichloroethylene photocatalytic degradation. *Appl. Surf. Sci.* **2016**, *384*, 192–199. [CrossRef]

52. Pipitone, G.; Tosches, D.; Bensaid, S.; Galia, A.; Pirone, R. Valorization of alginate for the production of hydrogen via catalytic aqueous phase reforming. *Catal. Today* **2018**, *304*, 153–164. [CrossRef]

53. Hibino, T.; Kobayashi, K.; Ito, M.; Nagao, M.; Fukui, M.; Teranishi, S. Direct electrolysis of waste newspaper for sustainable hydrogen production: An oxygen-functionalized porous carbon anode. *Appl. Catal. B Environ.* **2018**, *231*, 191–199. [CrossRef]

54. Park, S.; Kim, B.; Lee, Y.; Cho, M. Influence of copper electroplating on high pressure hydrogen-storage behaviors of activated carbon fibers. *Int. J. Hydrogen Energy* **2008**, *33*, 1706–1710. [CrossRef]

55. Im, J.S.; Park, S.-J.; Lee, Y.-S. Superior prospect of chemically activated electrospun carbon fibers for hydrogen storage. *Mater. Res. Bull.* **2009**, *44*, 1871–1878. [CrossRef]

56. Xiang, Q.; Yu, J. Graphene-Based Photocatalysts for Hydrogen Generation. *J. Phys. Chem. Lett.* **2013**, *4*, 753–759. [CrossRef]

57. Kim, H.-I.; Moon, G.-H.; Monllor-Satoca, D.; Park, Y.; Choi, W. Solar Photoconversion Using Graphene/TiO_2 Composites: Nanographene Shell on TiO_2 Core versus TiO_2 Nanoparticles on Graphene Sheet. *J. Phys. Chem. C* **2011**, *116*, 1535–1543. [CrossRef]

58. Wu, Z.; Zhou, Z.; Zhang, Y.; Wang, J.; Shi, H.; Shen, Q.; Wei, G.; Zhao, G. Simultaneous photoelectrocatalytic aromatic organic pollutants oxidation for hydrogen production promotion with a self-biasing photoelectrochemical cell. *Électrochim. Acta* **2017**, *254*, 140–147. [CrossRef]

59. Kim, B.J.; Lee, Y.S.; Park, S.J. Preparation of platinum-decorated porous graphite nanofibers, and their hydrogen storage behaviors. *J. Colloid Interface Sci.* **2008**, *318*, 530–533. [CrossRef]

60. Zhang, Y.; Park, S.-J. Fabrication and characterization of flower-like BiOI/Pt heterostructure with enhanced photocatalytic activity under visible light irradiation. *J. Solid State Chem.* **2017**, *253*, 421–429. [CrossRef]

61. Zhang, Y.; Park, S.-J. Incorporation of RuO_2 into charcoal-derived carbon with controllable microporosity by CO_2 activation for high-performance supercapacitor. *Carbon* **2017**, *122*, 287–297. [CrossRef]

62. Panthi, G.; Park, M.; Kim, H.-Y.; Park, S.-J. Electrospun polymeric nanofibers encapsulated with nanostructured materials and their applications: A review. *J. Ind. Eng. Chem.* **2015**, *24*, 1–13. [CrossRef]

63. Panthi, G.; Park, M.; Kim, H.-Y.; Lee, S.-Y.; Park, S.-J. Electrospun ZnO hybrid nanofibers for photodegradation of wastewater containing organic dyes: A review. *J. Ind. Eng. Chem.* **2015**, *21*, 26–35. [CrossRef]

64. Kim, S.; Park, S. Electroactivity of Pt–Ru/polyaniline composite catalyst-electrodes prepared by electrochemical deposition methods. *Solid State Ion.* **2008**, *178*, 1915–1921. [CrossRef]

65. Park, S.J.; Kim, B.J. Influence of oxygen plasma treatment on hydrogen chloride removal of activated carbon fibers. *J. Colloid Interface Sci.* **2004**, *275*, 590–595. [CrossRef] [PubMed]

66. Park, S.-J.; Kim, J.S. Modifications produced by electrochemical treatments oncarbon blacks Microstructures and mechanical interfacial properties. *Carbon* **2001**, *39*, 2011–2016. [CrossRef]

67. Chen, W.-T.; Chan, A.; Sun-Waterhouse, D.; Llorca, J.; Idriss, H.; Waterhouse, G.I.N. Performance comparison of Ni/TiO$_2$ and Au/TiO$_2$ photocatalysts for H$_2$ production in different alcohol-water mixtures. *J. Catal.* **2018**, *367*, 27–42. [CrossRef]

68. Hou, H.; Liu, H.; Gao, F.; Shang, M.; Wang, L.; Xu, L.; Wong, W.-Y.; Yang, W. Packaging BiVO$_4$ nanoparticles in ZnO microbelts for efficient photoelectrochemical hydrogen production. *Electrochim. Acta* **2018**, *283*, 497–508. [CrossRef]

69. Belhadj, H.; Hamid, S.; Robertson, P.K.J.; Bahnemann, D.W. Mechanisms of Simultaneous Hydrogen Production and Formaldehyde Oxidation in H$_2$O and D$_2$O over Platinized TiO$_2$. *ACS Catal.* **2017**, *7*, 4753–4758. [CrossRef]

70. Akbarzadeh, R.; Ghaedi, M.; Nasiri Kokhdan, S.; Jannesar, R.; Sadeghfar, F.; Sadri, F.; Tayebi, L. Electrochemical hydrogen storage, photocatalytical and antibacterial activity of Fe Ag bimetallic nanoparticles supported on TiO$_2$ nanowires. *Int. J. Hydrogen Energy* **2018**, *43*, 18316–18329. [CrossRef]

71. Chen, C.; Cai, W.M.; Long, M.C.; Zhou, B.X.; Wu, Y.H.; Wu, D.Y.; Feng, Y.J. Synthesis of Visible Light Responsive Graphene Oxide/ TiO$_2$ Composites with p/n Heterojunction. *ACS Nano* **2010**, *4*, 6425–6432. [CrossRef] [PubMed]

72. Cao, S.; Yu, J. g-C$_3$N$_4$-Based Photocatalysts for Hydrogen Generation. *J. Phys. Chem. Lett.* **2014**, *5*, 2101–2107. [CrossRef] [PubMed]

73. Rather, R.A.; Singh, S.; Pal, B. A C$_3$N$_4$ surface passivated highly photoactive Au-TiO$_2$ tubular nanostructure for the efficient H$_2$ production from water under sunlight irradiation. *Appl. Catal. B Environ.* **2017**, *213*, 9–17. [CrossRef]

74. Bian, H.; Ji, Y.; Yan, J.; Li, P.; Li, L.; Li, Y.; Frank Liu, S. In Situ Synthesis of Few-Layered g-C$_3$N$_4$ with Vertically Aligned MoS$_2$ Loading for Boosting Solar-to-Hydrogen Generation. *Small* **2018**, *14*, 1703003. [CrossRef] [PubMed]

75. Tian, N.; Zhang, Y.; Li, X.; Xiao, K.; Du, X.; Dong, F.; Waterhouse, G.I.N.; Zhang, T.; Huang, H. Precursor-reforming protocol to 3D mesoporous g-C$_3$N$_4$ established by ultrathin self-doped nanosheets for superior hydrogen evolution. *Nano Energy* **2017**, *38*, 72–81. [CrossRef]

76. Xu, X.; Si, Z.; Liu, L.; Wang, Z.; Chen, Z.; Ran, R.; He, Y.; Weng, D. CoMoS$_2$/rGO/C$_3$N$_4$ ternary heterojunctions catalysts with high photocatalytic activity and stability for hydrogen evolution under visible light irradiation. *Appl. Surf. Sci.* **2018**, *435*, 1296–1306. [CrossRef]

77. Luo, X.; Wu, Z.; Liu, Y.; Ding, S.; Zheng, Y.; Jiang, Q.; Zhou, T.; Hu, J. Engineering Amorphous Carbon onto Ultrathin g-C$_3$N$_4$ to Suppress Intersystem Crossing for Efficient Photocatalytic H$_2$ Evolution. *Adv. Mater. Interfaces* **2018**, *5*, 1800859. [CrossRef]

78. Wang, Y.; Wang, X.; Antonietti, M. Polymeric graphitic carbon nitride as a heterogeneous organocatalyst: From photochemistry to multipurpose catalysis to sustainable chemistry. *Angewandte Chem.* **2012**, *51*, 68–89. [CrossRef]

79. Wang, X.; Maeda, K.; Thomas, A.; Takanabe, K.; Xin, G.; Carlsson, J.M.; Domen, K.; Antonietti, M. A metal-free polymeric photocatalyst for hydrogen production from water under visible light. *Nat. Mater.* **2009**, *8*, 76–80. [CrossRef]

80. Gao, H.; Yang, H.; Xu, J.; Zhang, S.; Li, J. Strongly Coupled g-C$_3$N$_4$ Nanosheets-Co$_3$O$_4$ Quantum Dots as 2D/0D Heterostructure Composite for Peroxymonosulfate Activation. *Small* **2018**, *14*, 1801353. [CrossRef]

81. Chen, Z.; Xia, K.; She, X.; Mo, Z.; Zhao, S.; Yi, J.; Xu, Y.; Chen, H.; Xu, H.; Li, H. 1D metallic MoO$_2$-C as co-catalyst on 2D g-C$_3$N$_4$ semiconductor to promote photocatlaytic hydrogen production. *Appl. Surf. Sci.* **2018**, *447*, 732–739. [CrossRef]

82. Kong, L.; Ji, Y.; Dang, Z.; Yan, J.; Li, P.; Li, Y.; Liu, S.F. g-C$_3$N$_4$ Loading Black Phosphorus Quantum Dot for Efficient and Stable Photocatalytic H2 Generation under Visible Light. *Adv. Funct. Mater.* **2018**, *28*, 1800668. [CrossRef]

83. Wan, J.; Pu, C.; Wang, R.; Liu, E.; Du, X.; Bai, X.; Fan, J.; Hu, X. A facile dissolution strategy facilitated by H_2SO_4 to fabricate a 2D metal-free g-C_3N_4/rGO heterojunction for efficient photocatalytic H_2 production. *Int. J. Hydrogen Energy* **2018**, *43*, 7007–7019. [CrossRef]

84. Marcì, G.; García-López, E.I.; Palmisano, L. Polymeric carbon nitride (C_3N_4) as heterogeneous photocatalyst for selective oxidation of alcohols to aldehydes. *Catal. Today* **2018**, *315*, 126–137. [CrossRef]

85. Oh, W.-D.; Lok, L.-W.; Veksha, A.; Giannis, A.; Lim, T.-T. Enhanced photocatalytic degradation of bisphenol A with Ag-decorated S-doped g-C_3N_4 under solar irradiation: Performance and mechanistic studies. *Chem. Eng. J.* **2018**, *333*, 739–749. [CrossRef]

86. Hou, Y.; Laursen, A.B.; Zhang, J.; Zhang, G.; Zhu, Y.; Wang, X.; Dahl, S.; Chorkendorff, I. Layered nanojunctions for hydrogen-evolution catalysis. *Angewandte Chem.* **2013**, *52*, 3621–3625. [CrossRef] [PubMed]

87. Zhou, J.; Zhao, Y.; Bao, J.; Huo, D.; Fa, H.; Shen, X.; Hou, C. One-step electrodeposition of Au-Pt bimetallic nanoparticles on MoS_2 nanoflowers for hydrogen peroxide enzyme-free electrochemical sensor. *Electrochim. Acta* **2017**, *250*, 152–158. [CrossRef]

88. Yang, Y.; Gao, P.; Ren, X.; Sha, L.; Yang, P.; Zhang, J.; Chen, Y.; Yang, L. Massive Ti^{3+} self-doped by the injected electrons from external Pt and the efficient photocatalytic hydrogen production under visible-Light. *Appl. Catal. B Environ.* **2017**, *218*, 751–757. [CrossRef]

89. Fang, J.; Gu, J.; Liu, Q.; Zhang, W.; Su, H.; Zhang, D. Three-Dimensional CdS/Au Butterfly Wing Scales with Hierarchical Rib Structures for Plasmon-Enhanced Photocatalytic Hydrogen Production. *ACS Appl. Mater. Interfaces* **2018**, *10*, 19649–19655. [CrossRef] [PubMed]

90. Chang, Y.; Yu, K.; Zhang, C.; Yang, Z.; Feng, Y.; Hao, H.; Jiang, Y.; Lou, L.-L.; Zhou, W.; Liu, S. Ternary CdS/Au/3DOM-$SrTiO_3$ composites with synergistic enhancement for hydrogen production from visible-light photocatalytic water splitting. *Appl. Catal. B Environ.* **2017**, *215*, 74–84. [CrossRef]

91. Masudy-Panah, S.; Siavash Moakhar, R.; Chua, C.S.; Kushwaha, A.; Dalapati, G.K. Stable and Efficient CuO Based Photocathode through Oxygen-Rich Composition and Au-Pd Nanostructure Incorporation for Solar-Hydrogen Production. *ACS Appl. Mater. Interfaces* **2017**, *9*, 27596–27606. [CrossRef] [PubMed]

92. Ortiz, N.; Zoellner, B.; Hong, S.J.; Ji, Y.; Wang, T.; Liu, Y.; Maggard, P.A.; Wang, G. Harnessing Hot Electrons from Near IR Light for Hydrogen Production Using Pt-End-Capped-AuNRs. *ACS Appl. Mater. Interfaces* **2017**, *9*, 25962–25969. [CrossRef]

93. Wang, Y.; Zhao, J.; Li, Y.; Wang, C. Selective photocatalytic CO_2 reduction to CH_4 over Pt/In_2O_3: Significant role of hydrogen adatom. *Appl. Catal. B Environ.* **2018**, *226*, 544–553. [CrossRef]

94. Jiang, J.-Z.; Ren, L.-Q.; Huang, Y.-P.; Li, X.-D.; Wu, S.-H.; Sun, J.-J. 3D Nanoporous Gold-Supported Pt Nanoparticles as Highly Accelerating Catalytic Au-Pt Micromotors. *Adv. Mater. Interfaces* **2018**, *5*, 1701689. [CrossRef]

95. Lang, Q.; Chen, Y.H.; Huang, T.L.; Yang, L.N.; Zhong, S.X.; Wu, L.J.; Chen, J.R.; Bai, S. Graphene 'bridge' in transferring hot electrons from plasmonic Ag nanocubes to TiO_2 nanosheets for enhanced visible light photocatalytic hydrogen evolution. *Appl. Catal. B Environ.* **2018**, *220*, 182–190. [CrossRef]

96. Zhang, Y.; Park, S.-J. Facile construction of MoO_3@ZIF-8 core-shell nanorods for efficient photoreduction of aqueous Cr (VI). *Appl. Catal. B Environ.* **2019**, *240*, 92–101. [CrossRef]

97. Kamijyo, K.; Takashima, T.; Yoda, M.; Osaki, J.; Irie, H. Facile synthesis of a red light-inducible overall water-splitting photocatalyst using gold as a solid-state electron mediator. *Chem. Commun.* **2018**, *54*, 7999–8002. [CrossRef] [PubMed]

98. Maeda, K.; Domen, K. Photocatalytic Water Splitting: Recent Progress and Future Challenges. *J. Phys. Chem. Lett.* **2010**, *1*, 2655–2661. [CrossRef]

99. Iwase, A.; Ng, Y.H.; Ishiguro, Y.; Kudo, A.; Amal, R. Reduced graphene oxide as a solid-state electron mediator in Z-scheme photocatalytic water splitting under visible light. *J. Am. Chem. Soc.* **2011**, *133*, 11054–11057. [CrossRef] [PubMed]

100. Zhang, Y.; Park, S.-J. Formation of hollow MoO_3/SnS_2 heterostructured nanotubes for efficient light-driven hydrogen peroxide production. *J. Mater. Chem. A* **2018**, *6*, 20304–20312. [CrossRef]

101. Xu, C.; Qiu, P.; Li, L.; Chen, H.; Jiang, F.; Wang, X. Bismuth Subcarbonate with Designer Defects for Broad-Spectrum Photocatalytic Nitrogen Fixation. *ACS Appl. Mater. Interfaces* **2018**, *10*, 25321–25328. [CrossRef] [PubMed]

102. Kobayashi, R.; Takashima, T.; Tanigawa, S.; Takeuchi, S.; Ohtani, B.; Irie, H. A heterojunction photocatalyst composed of zinc rhodium oxide, single crystal-derived bismuth vanadium oxide, and silver for overall pure-water splitting under visible light up to 740 nm. *Phys. Chem. Chem. Phys. PCCP* **2016**, *18*, 27754–27760. [CrossRef] [PubMed]

103. Iwashina, K.; Iwase, A.; Ng, Y.H.; Amal, R.; Kudo, A. Z-schematic water splitting into H_2 and O_2 using metal sulfide as a hydrogen-evolving photocatalyst and reduced graphene oxide as a solid-state electron mediator. *J. Am. Chem. Soc.* **2015**, *137*, 604–607. [CrossRef] [PubMed]

104. Yu, X.; Liu, G.; Li, W.; An, L.; Li, Z.; Liu, J.; Hu, P. Mesocrystalline Ta_2O_5 nanosheets supported Pd Pt nanoparticles for efficient photocatalytic hydrogen production. *Int. J. Hydrogen Energy* **2018**, *43*, 8232–8242. [CrossRef]

105. Low, J.; Yu, J.; Jaroniec, M.; Wageh, S.; Al-Ghamdi, A.A. Heterojunction Photocatalysts. *Adv. Mater.* **2017**, *29*, 1601694. [CrossRef] [PubMed]

106. Zhu, M.; Zhai, C.; Fujitsuka, M.; Majima, T. Noble metal-free near-infrared-driven photocatalyst for hydrogen production based on 2D hybrid of black Phosphorus/WS_2. *Appl. Catal. B Environ.* **2018**, *221*, 645–651. [CrossRef]

107. Do, J.Y.; Lee, J.H.; Park, N.-K.; Lee, T.J.; Lee, S.T.; Kang, M. Synthesis and characterization of $Ni_{2-x}Pd_xMnO_4/\gamma$-Al_2O_3 catalysts for hydrogen production via propane steam reforming. *Chem. Eng. J.* **2018**, *334*, 1668–1678. [CrossRef]

108. Qin, Z.; Xue, F.; Chen, Y.; Shen, S.; Guo, L. Spatial charge separation of one-dimensional Ni_2P-$Cd_{0.9}Zn_{0.1}S$/g-C_3N_4 heterostructure for high-quantum-yield photocatalytic hydrogen production. *Appl. Catal. B Environ.* **2017**, *217*, 551–559. [CrossRef]

109. Hu, Z.; Wang, X.; Dong, H.; Li, S.; Li, X.; Li, L. Efficient photocatalytic degradation of tetrabromodiphenyl ethers and simultaneous hydrogen production by TiO_2-Cu_2O composite films in N_2 atmosphere: Influencing factors, kinetics and mechanism. *J. Hazard. Mater.* **2017**, *340*, 1–15. [CrossRef]

110. Iervolino, G.; Vaiano, V.; Sannino, D.; Rizzo, L.; Galluzzi, A.; Polichetti, M.; Pepe, G.; Campiglia, P. Hydrogen production from glucose degradation in water and wastewater treated by Ru-$LaFeO_3$/Fe_2O_3 magnetic particles photocatalysis and heterogeneous photo-Fenton. *Int. J. Hydrogen Energy* **2018**, *43*, 2184–2196. [CrossRef]

111. Imran, M.; Yousaf, A.B.; Kasak, P.; Zeb, A.; Zaidi, S.J. Highly efficient sustainable photocatalytic Z-scheme hydrogen production from an α-Fe_2O_3 engineered ZnCdS heterostructure. *J. Catal.* **2017**, *353*, 81–88. [CrossRef]

112. Subha, N.; Mahalakshmi, M.; Myilsamy, M.; Neppolian, B.; Murugesan, V. Direct Z-scheme heterojunction nanocomposite for the enhanced solar H_2 production. *Appl. Catal. A Gen.* **2018**, *553*, 43–51. [CrossRef]

113. Zhang, J.; Yan, W.; An, Z.; Song, H.; He, J. Interface–Promoted Dehydrogenation and Water–Gas Shift toward High-Efficient H_2 Production from Aqueous Phase Reforming of Cellulose. *ACS Sustain. Chem. Eng.* **2018**, *6*, 7313–7324. [CrossRef]

114. Vinodgopal, K.; Kamat, P.V. Enhanced rates of photocatalytic degradation of an azo dye using SnO_2/TiO_2 coupled semiconductor thin films. *Environ. Sci. Technol.* **1995**, *29*, 841–845. [CrossRef] [PubMed]

115. Ranjit, K.; Viswanathan, B. Synthesis, characterization and photocatalytic properties of iron-doped TiO_2 catalysts. *J. Photochem. Photobiol. A* **1997**, *108*, 79–84. [CrossRef]

116. Monai, M.; Montini, T.; Fonda, E.; Crosera, M.; Delgado, J.J.; Adami, G.; Fornasiero, P. Nanostructured Pd Pt nanoparticles: Evidences of structure/performance relations in catalytic H_2 production reactions. *Appl. Catal. B Environ.* **2018**, *236*, 88–98. [CrossRef]

117. Wang, Q.; He, J.; Shi, Y.; Zhang, S.; Niu, T.; She, H.; Bi, Y.; Lei, Z. Synthesis of MFe_2O_4 (M = Ni, Co)/$BiVO_4$ film for photoelectrochemical hydrogen production activity. *Appl. Catal. B Environ.* **2017**, *214*, 158–167. [CrossRef]

118. Xu, J.; Gao, J.; Qi, Y.; Wang, C.; Wang, L. Anchoring Ni_2P on the UiO-66-NH_2/g-C_3N_4-derived C-doped ZrO_2/g-C_3N_4 Heterostructure: Highly Efficient Photocatalysts for H_2 Production from Water Splitting. *ChemCatChem* **2018**, *10*, 3327–3335. [CrossRef]

119. Wang, Z.; Jin, Z.; Wang, G.; Ma, B. Efficient hydrogen production over MOFs (ZIF-67) and g-C_3N_4 boosted with MoS_2 nanoparticles. *Int. J. Hydrogen Energy* **2018**, *43*, 13039–13050. [CrossRef]

120. Fu, J.; Zhu, B.; You, W.; Jaroniec, M.; Yu, J. A flexible bio-inspired H_2- production photocatalyst. *Appl. Catal. B Environ.* **2018**, *220*, 148–160. [CrossRef]

121. Zhang, S.; Liu, X.; Liu, C.; Luo, S.; Wang, L.; Cai, T.; Zeng, Y.; Yuan, J.; Dong, W.; Pei, Y.; et al. MoS$_2$ Quantum Dot Growth Induced by S Vacancies in a ZnIn$_2$S$_4$ Monolayer: Atomic-Level Heterostructure for Photocatalytic Hydrogen Production. *ACS Nano* **2018**, *12*, 751–758. [CrossRef] [PubMed]

122. Li, K.; Gao, S.; Wang, Q.; Xu, H.; Wang, Z.; Huang, B.; Dai, Y.; Lu, J. In-Situ-Reduced Synthesis of Ti(3)(+) Self-Doped TiO($_2$)/g-C($_3$)N($_4$) Heterojunctions with High Photocatalytic Performance under LED Light Irradiation. *ACS Appl. Mater. Interfaces* **2015**, *7*, 9023–9030. [CrossRef] [PubMed]

123. Hong, S.J.; Lee, S.; Jang, J.S.; Lee, J.S. Heterojunction BiVO$_4$/WO$_3$ electrodes for enhanced photoactivity of water oxidation. *Energy Environ. Sci.* **2011**, *4*, 1781–1787. [CrossRef]

124. Huang, L.; Xu, H.; Li, Y.; Li, H.; Cheng, X.; Xia, J.; Xu, Y.; Cai, G. Visible-light-induced WO$_3$/g-C$_3$N$_4$ composites with enhanced photocatalytic activity. *Dalton Trans.* **2013**, *42*, 8606–8616. [CrossRef] [PubMed]

125. Pan, C.; Xu, J.; Wang, Y.; Li, D.; Zhu, Y. Dramatic Activity of C$_3$N$_4$/BiPO$_4$ Photocatalyst with Core/Shell Structure Formed by Self-Assembly. *Adv. Funct. Mater.* **2012**, *22*, 1518–1524. [CrossRef]

126. Zhang, J.; Qiao, S.Z.; Qi, L.; Yu, J. Fabrication of NiS modified CdS nanorod p-n junction photocatalysts with enhanced visible-light photocatalytic H$_2$-production activity. *Phys. Chem. Chem. Phys. PCCP* **2013**, *15*, 12088–12094. [CrossRef]

127. Heo, Y.-J.; Zhang, Y.; Rhee, K.Y.; Park, S.-J. Synthesis of PAN/PVDF nanofiber composites-based carbon adsorbents for CO$_2$ capture. *Compos. Part B Eng.* **2019**, *156*, 95–99. [CrossRef]

128. Zhang, Y.; Park, M.; Kim, H.Y.; Park, S.J. Moderated surface defects of Ni particles encapsulated with NiO nanofibers as supercapacitor with high capacitance and energy density. *J. Colloid Interface Sci.* **2017**, *500*, 155–163. [CrossRef]